J. Fluid Mech. (1998), *vol.* 361, *pp.* 117–143. Printed in the United Kingdom

Deformation of liquid capsules enclosed by elastic membranes in simple shear flow: large deformations and the effect of fluid viscosities

By S. RAMANUJAN[1] AND C. POZRIKIDIS[2]

[1]Department of Chemical Engineering, University of Wisconsin at Madison, Madison, WI 53706-1691, USA

[2]Department of Applied Mechanics and Engineering Sciences, University of California at San Diego, La Jolla, CA 92093-0411, USA

(Received 27 August 1997 and in revised form 3 December 1997)

The deformation of a liquid capsule enclosed by an elastic membrane in an infinite simple shear flow is studied numerically at vanishing Reynolds numbers using a boundary-element method. The surface of the capsule is discretized into quadratic triangular elements that form an evolving unstructured grid. The elastic membrane tensions are expressed in terms of the surface deformation gradient, which is evaluated from the position of the grid points. Compared to an earlier formulation that uses global curvilinear coordinates, the triangular-element formulation suppresses numerical instabilities due to uneven discretization and thus enables the study of large deformations and the investigation of the effect of fluid viscosities. Computations are performed for capsules with spherical, spheroidal, and discoidal unstressed shapes over an extended range of the dimensionless shear rate and for a broad range of the ratio of the internal to surrounding fluid viscosities. Results for small deformations of spherical capsules are in quantitative agreement with the predictions of perturbation theories. Results for large deformations of spherical capsules and deformations of non-spherical capsules are in qualitative agreement with experimental observations of synthetic capsules and red blood cells. We find that initially spherical capsules deform into steady elongated shapes whose aspect ratios increase with the magnitude of the shear rate. A critical shear rate above which capsules exhibit continuous elongation is not observed for any value of the viscosity ratio. This behaviour contrasts with that of liquid drops with uniform surface tension and with that of axisymmetric capsules subject to a stagnation-point flow. When the shear rate is sufficiently high and the viscosity ratio is sufficiently low, liquid drops exhibit continuous elongation leading to breakup. Axisymmetric capsules deform into thinning needles at sufficiently high rates of elongation, independent of the fluid viscosities. In the case of capsules in shear flow, large elastic tensions develop at large deformations and prevent continued elongation, stressing the importance of the vorticity of the incident flow. The long-time behaviour of deformed capsules depends strongly on the unstressed shape. Oblate capsules exhibit unsteady motions including oscillation about a mean configuration at low viscosity ratios and continuous rotation accompanied by periodic deformation at high viscosity ratios. The viscosity ratio at which the transition from oscillations to tumbling occurs decreases with the sphericity of the unstressed shape. Results on the effective rheological properties of dilute suspensions confirm a non-Newtonian shear-thinning behaviour.

1. Introduction

In the past two decades, considerable effort has been devoted to modelling and simulating the motion of flexible particles in Stokes flow. This work has been motivated by numerous applications in the fields of particulate flow and biofluid-dynamics, such as emulsion rheology and blood flow. Theoretical advances, including the development of compact mathematical formulations and sophisticated boundary integral algorithms, have allowed significant progress in the computational approaches relevant to these applications. Liquid drops with uniform or variable isotropic surface tension have received special attention. Solitary and collective drop configurations have been studied extensively, and current efforts are directed toward the simulation of emulsion flows with numerous suspended particles (Li, Charles & Pozrikidis 1996; Loewenberg & Hinch 1996; Charles & Pozrikidis 1998).

Some progress has also been made in the simulation of liquid capsules with more complicated interfacial behaviours. The Newtonian interface model introduced by Boussinésq (1913) and further developed by Scriven (1960) incorporates isotropic tension, regarded as the analogue of thermodynamic pressure, and viscous surface tensions that depend linearly on the interfacial rate of deformation; generalization to nonlinear interfacial behaviours is straightforward. The Boussinésq–Scriven model is applicable to interfaces with impurities and large concentrations of surfactants. Pozrikidis (1994) extended prior asymptotic theories by performing a numerical study of the finite deformation of drops with constant surface tension and viscous interfacial tensions. Shrivatsava & Tang (1993) also considered surface viscosity effects in a finite-element study of the inflation of viscoelastic membranes in thermoforming.

Several types of capsules encountered in industrial or biomedical settings are liquid drops enclosed by membranes with elastic characteristics. Examples include synthetic capsules with polymerized interfaces and red blood cells. The red blood cell consists of a Newtonian hemoglobin solution encapsulated by a bilayer membrane and a thin protein skeleton (Evans & Skalak 1980). Unlike most biological cells, the red cell has no internal structure and lacks a nucleus. Efforts to model white blood cells as elastic bodies or multi-layered capsules have failed to reproduce experimental observations with adequate accuracy; the development of appropriate models is under continued investigation (Skalak, Dong & Zhu 1990). Thus, while a capsule model may be relevant, a strong claim regarding its ability to describe white blood cell behaviour cannot be made.

Asymptotic theories describing small deformations of elastic capsules were developed by Barthès-Biesel and coworkers (Barthès-Biesel 1980; Barthès-Biesel & Rallison 1981; Barthès-Biesel & Sgaier 1985), and numerical simulations of large axisymmetric capsule deformations were presented by Li, Barthès-Biesel & Helmy (1988). The numerical studies considered deformations of capsules with spherical, oblate, and prolate shapes subject to axisymmetric straining flow, establishing the existence of a critical strain rate above which the capsule continues to elongate without reaching a steady asymptotic shape. This intriguing behaviour is seemingly counterintuitive, as we expect that strong elastic tensions produced by large deformations will limit the elongation. We shall address the existence of critical conditions more thoroughly in a later section. More recently, Leyrat-Maurin, Drochon & Barthès-Biesel (1993) and Leyrat-Maurin & Barthès-Biesel (1994) simulated the axisymmetric motion of elastic capsules through tubes and constrictions and established critical conditions for pore occlusion. Pozrikidis (1995) developed a method for simulating three-dimensional deformations and presented results for capsules with spherical unstressed shapes subject

to simple shear flow. In all of these numerical studies, in order to reduce the computational cost, the viscosity of the capsule fluid was assumed to match that of the ambient fluid. Laboratory observations of synthetic capsules were reported by Chang & Olbricht (1993*a*, *b*). Apart from these hydrodynamic investigations, there have been many experimental observations of red blood cell deformations in viscometric and capillary shear flows.

Although a reasonable starting point, the numerical method used by Pozrikidis (1995) has several shortcomings that limited the breadth and depth of his investigations. In his method, the interface is described by two global surface curvilinear coordinates that emanate from two singular points. The size of the boundary elements decreases rapidly near the singular points, causing numerical instability during the transient deformation. Furthermore, the global discretization performs poorly for complex shapes such as biconcave disks, and maintaining regularity by regridding requires further numerical progress. Fortunately, these problems can be minimized through the use of an unstructured grid of quadratic triangular elements, similar to that used by Kennedy, Pozrikidis & Skalak (1994) for the simulation of liquid drops.

Our two primary objectives in this work are as follows. First, we develop and evaluate a method of computing the elastic tensions at the nodes of an unstructured triangular grid describing the capsule membrane. The marker points defining the grid are not necesarily material points, but may execute an arbitrary tangential motion. Incorporating this method into the standard boundary-integral formulation, we obtain a procedure that is superior to that used by Pozrikidis (1995). Second, we investigate large capsule deformations for a variety of unstressed shapes, considering cases where the internal viscosity of the capsule is different than that of the ambient fluid. We characterize the behavioural modes observed and estimate the effective rheological properties of dilute suspensions. The ability to compute large deformations allows us to correct an erroneous conclusion drawn by Pozrikidis (1995) regarding the existence of critical conditions for contined elongation. Finally, we compare our numerical results with published experimental data for synthetic capsules and red blood cells and find satisfactory agreement.

2. Problem formulation

We consider the deformation of a liquid capsule suspended in an infinite ambient fluid with viscosity μ, subject to an infinite simple shear flow with velocity $\boldsymbol{v}^{\infty}(x, y, z) = (ky, 0, 0)$, as shown in figure 1. The capsule contains a Newtonian fluid with viscosity $\lambda\mu$ and is bounded by an elastic membrane S with infinitesimal thickness and negligible resistance to bending. The precise mechanical properties of the membrane will be specified later in this section. The capsule and ambient fluid densities are assumed equal, so that the capsule is neutrally buoyant. For future reference, we label the ambient fluid as fluid 1 and the capsule fluid as fluid 2.

The size of the capsule is assumed to be sufficiently small so that the Reynolds number of the flow is negligible and the motion of the fluid inside and outside the capsule is governed by the equations of Stokes flow. These include the continuity equation for incompressible fluids, $\nabla \cdot \boldsymbol{v}^{(i)} = 0$, and the linearized equation of motion, $-\nabla p^{(i)} + \mu_i \nabla^2 \boldsymbol{v}^{(i)} = \boldsymbol{0}$, where $\mu_i = \mu$ for the external flow and $\lambda\mu$ for the internal flow. We assume the interface has a simple structure, so that the fluid velocity is identical on either side: for $\boldsymbol{x} \in S$, $\boldsymbol{v}^{(1)}(\boldsymbol{x}) = \boldsymbol{v}^{(2)}(\boldsymbol{x})$. The hydrodynamic traction exerted on either

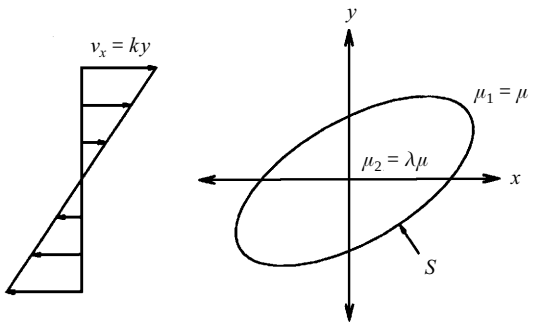

FIGURE 1. Schematic diagram of capsule in shear flow.

side of the interface at the point $\boldsymbol{x}_m$, however, undergoes a discontinuity,

$$\Delta \boldsymbol{f} = (\boldsymbol{\sigma}^{(1)} - \boldsymbol{\sigma}^{(2)}) \cdot \boldsymbol{n} \tag{2.1}$$

where $\boldsymbol{\sigma}^{(i)}$ is the stress tensor of fluid i at $\boldsymbol{x}$, and $\boldsymbol{n}$ is the unit vector normal to the interface, pointing into the ambient fluid. A differential balance of the hydrodynamic and elastic tensions on an infinitesimal section of the interface yields a relation between $\Delta \boldsymbol{f}$ and the membrane tension tensor $\boldsymbol{T}$,

$$\Delta \boldsymbol{f} = \nabla^s \cdot \boldsymbol{T}. \tag{2.2}$$

The surface divergence operator is defined in terms of the normal vector as $\nabla^s = (\boldsymbol{I} - \boldsymbol{nn}) \cdot \nabla$, where $\boldsymbol{I}$ is the identity tensor.

To complete the mathematical formulation, we must introduce an elastic constitutive equation that expresses the membrane tensions in terms of the interfacial deformation. We follow standard procedure (Beatty 1987) and consider the position vector $\boldsymbol{X}$ of a point particle on the interface in the unstressed state, and the position $\boldsymbol{x}$ after deformation. To develop a theory of elasticity for a three-dimensional solid, we introduce the deformation gradient $\boldsymbol{F}$, defined as

$$\boldsymbol{F}(\boldsymbol{X}, t) = \frac{\partial \boldsymbol{x}(\boldsymbol{X}, t)}{\partial \boldsymbol{X}}. \tag{2.3}$$

To model membrane tensions, we follow the alternative approach of Barthès-Biesel & Rallison (1981) and introduce the surface deformation gradient

$$\boldsymbol{A} = (\boldsymbol{I} - \boldsymbol{nn}) \cdot \boldsymbol{F} \cdot (\boldsymbol{I} - \boldsymbol{NN}), \tag{2.4}$$

where $\boldsymbol{N}$ denotes the unit vector normal to the undeformed surface. Note that the projections of a tangent vector on $\boldsymbol{A}$ and $\boldsymbol{F}$ are identical ($\mathrm{d}\boldsymbol{x} = \boldsymbol{A} \cdot \mathrm{d}\boldsymbol{X} = \boldsymbol{F} \cdot \mathrm{d}\boldsymbol{X}$ when $\mathrm{d}\boldsymbol{X} \cdot \boldsymbol{N} = 0$), whereas the projection of a normal vector on $\boldsymbol{A}$ vanishes ($\boldsymbol{A} \cdot \boldsymbol{N} = \boldsymbol{0}$). Thus, the surface deformation gradient tensor $\boldsymbol{A}$ is singular with the zero eigenvalue corresponding to the eigenvector $\boldsymbol{N}$. We proceed by defining the stretch tensor $\boldsymbol{\Lambda}$ and the left Cauchy-Green strain tensor $\boldsymbol{B}$,

$$\boldsymbol{B} = \boldsymbol{\Lambda}^2 = \boldsymbol{A} \cdot \boldsymbol{A}^T. \tag{2.5}$$

The eigenvalues λ_i of $\boldsymbol{\Lambda}$ are the principal extension ratios of the interface at a point. Barthès-Biesel & Rallison (1981) introduced the strain invariants

$$\Lambda_1 = \log \lambda_1 \lambda_2 = \tfrac{1}{2} \log \left\{ \tfrac{1}{2} [\mathrm{tr}(\boldsymbol{B})^2 - \mathrm{tr}(\boldsymbol{B}^2)] \right\}, \tag{2.6a}$$

$$\Lambda_2 = \tfrac{1}{2}(\lambda_1{}^2 + \lambda_2{}^2) - 1 = \tfrac{1}{2} \mathrm{tr}\, \boldsymbol{B} - 1, \tag{2.6b}$$

and derived the following relationship between the Cauchy stresses and the surface strain energy function $W(\Lambda_1, \Lambda_2)$ for a hyperelastic material:

$$\boldsymbol{T} = \mathrm{e}^{-\Lambda_1}\left[\frac{\partial W}{\partial \Lambda_1}(\boldsymbol{I} - \boldsymbol{nn}) + \frac{\partial W}{\partial \Lambda_2}\boldsymbol{B}\right]. \tag{2.7}$$

Note that the strain energy does not depend on λ_3 explicitly; instead, it is determined by λ_1 and λ_2 through a constitutive assumption of the form $\lambda_3 = \lambda_3(\lambda_1, \lambda_2)$. Treating the thin membrane as the zero-thickness limit of a three-dimensional isotropic incompressible elastic shell and expanding W in a McLaurin series with respect to the strain invariants, we obtain

$$W = c + \frac{Eh}{3}[-\Lambda_1 + \Lambda_2 + \Lambda_1^2 + \ldots], \tag{2.8}$$

where c is an arbitrary constant, h is the membrane thickness, and E is the bulk Young modulus of the three-dimensional elastic material (Barthès-Biesel & Rallison 1981). The surface elastic modulus for an elastic membrane is related to the bulk modulus by $E_s = Eh$.

Alternative constitutive equations for hyperelastic materials, such as Mooney elastic solids or biological membranes, may be used. For example, elastomeric behaviour is described by the Mooney–Rivlin strain energy function. For a thin membrane,

$$W = \frac{E_s}{6}(1 - \psi')[2\Lambda_2 + \mathrm{e}^{-2\Lambda_2} - 1] + \frac{E_s}{6}\psi'[2\Lambda_2\mathrm{e}^{-2\Lambda_1} + 2\mathrm{e}^{-2\Lambda_1} + \mathrm{e}^{2\Lambda_1} - 3], \tag{2.9}$$

where the dimensionless parameter $\psi' \in [0, 1]$ introduces nonlinear behaviour (Li *et al.* 1988). When $\psi' = 0$, the second term in (2.9) vanishes and the membrane is known as a neohookean elastic. To describe the elastic behaviour of the red cell membrane, which easily undergoes shear deformation but strongly resists local and global dilatation, Skalak *et al.* (1973) proposed the strain energy function

$$W = \frac{B}{4}[2\Lambda_2(\Lambda_2 + 1) + 1 - \mathrm{e}^{2\Lambda_2}] + \frac{C}{8}[\mathrm{e}^{2\Lambda_1} - 1]^2, \tag{2.10}$$

where $B \ll C$.

Having made a choice for W, we have a complete system of governing equations and accompanying boundary conditions. To compute the capsule deformation, we must determine the interfacial velocity field. We use a well-established formalism (Pozrikidis 1992) and derive the integral equation

$$\begin{aligned}\boldsymbol{v}(\boldsymbol{x}_0) = {} & \frac{2}{(\lambda+1)}\boldsymbol{v}^{\infty} - \frac{1}{4\pi\mu(\lambda+1)}\int_S \Delta\boldsymbol{f}(\boldsymbol{x})\cdot\boldsymbol{G}(\boldsymbol{x},\boldsymbol{x}_0)\,\mathrm{d}S_p(\boldsymbol{x}) \\ & + \frac{1-\lambda}{4\pi(1+\lambda)}\int_S \boldsymbol{v}(\boldsymbol{x})\cdot\boldsymbol{\Sigma}(\boldsymbol{x},\boldsymbol{x}_0)\cdot\boldsymbol{n}(\boldsymbol{x})\,\mathrm{d}S_p(\boldsymbol{x})\end{aligned} \tag{2.11}$$

for the interfacial velocity $\boldsymbol{v}$ at the point $\boldsymbol{x}_0$ that lies in the interface. The first and second integrals on the right-hand side are respectively the single-layer potential and the principal value of the double-layer potential of Stokes flow. The free-space Green's function and associated stress field are given by

$$\boldsymbol{G}(\boldsymbol{x},\boldsymbol{x}_0) = \frac{1}{r}\boldsymbol{I} + \frac{(\boldsymbol{x}-\boldsymbol{x}_0)(\boldsymbol{x}-\boldsymbol{x}_0)}{r^3}, \tag{2.12a}$$

$$\boldsymbol{\Sigma}(\boldsymbol{x},\boldsymbol{x}_0) = -6\frac{(\boldsymbol{x}-\boldsymbol{x}_0)(\boldsymbol{x}-\boldsymbol{x}_0)(\boldsymbol{x}-\boldsymbol{x}_0)}{r^5}, \tag{2.12b}$$

where $r = |\boldsymbol{x} - \boldsymbol{x}_0|$. When the internal and external fluid viscosities are equal ($\lambda = 1$), the double-layer term disappears. More generally, having computed $\Delta \boldsymbol{f}$ from (2.2), we obtain a Fredholm integral equation of the second kind for the interfacial velocity. In §3, we discuss the numerical evaluation of $\Delta \boldsymbol{f}$ and the solution of the integral equation using a boundary-element method.

To identify the parameters affecting the capsule deformation, we recast the governing equations and boundary conditions in dimensionless form. Lengths are scaled by the particle radius a, time by k^{-1}, velocities by ka, fluid stresses by μk, and interfacial stresses by an appropriate surface elastic modulus, Eh or E_s for three- and two-dimensional elastics respectively.

In terms of dimensionless variables indicated by an asterisk, the boundary-integral equation (2.11) becomes

$$\boldsymbol{v}^*(\boldsymbol{x}_0^*) = \frac{2}{(1+\lambda)}\boldsymbol{v}^{\infty *}(\boldsymbol{x}_0^*) - \frac{G}{4\pi(\lambda+1)}\int_S \Delta \boldsymbol{f}^*(\boldsymbol{x}) \cdot \boldsymbol{G}(\boldsymbol{x}^*, \boldsymbol{x}_0^*)\, \mathrm{d}S_p^*(\boldsymbol{x}^*) + \frac{1-\lambda}{4\pi(1+\lambda)}\int_S \boldsymbol{v}^*(\boldsymbol{x}^*) \cdot \boldsymbol{\Sigma}(\boldsymbol{x}^*, \boldsymbol{x}_o^*) \cdot \boldsymbol{n}(\boldsymbol{x}^*)\, \mathrm{d}S_p^*(\boldsymbol{x}^*). \tag{2.13}$$

The dimensionless shear rate,

$$G = \mu k a / E_s, \tag{2.14}$$

expresses the ratio of external viscous deforming stresses to restoring elastic tensions and is the counterpart of the capillary number, $Ca = \mu k a/\gamma$, associated with drops with constant surface tension γ. Equation (2.13) shows that the drop deformation is determined by the dimensionless shear rate G and the viscosity ratio λ, the two parameters of our problem. The significance of their roles will be assessed in the numerical investigations.

Considering now a dilute suspension, we neglect interparticle hydrodynamic interactions and express the effective rheological properties in terms of the flow past an isolated particle (Pozrikidis 1992). Pozrikidis (1995) showed that the effective stress tensor of a dilute suspension can be recast into the form

$$\langle \boldsymbol{\sigma} \rangle = -\boldsymbol{\delta}\langle P \rangle + 2\mu \langle \boldsymbol{e} \rangle + \Phi \int_S \{(\Delta \boldsymbol{f})\boldsymbol{x} - \mu(1-\lambda)(\boldsymbol{v}\boldsymbol{n} + \boldsymbol{n}\boldsymbol{v})\}\, \mathrm{d}S_p, \tag{2.15}$$

where Φ is the number density of particles, P is the pressure, $\boldsymbol{e}$ is the rate of strain tensor, and $\langle\ \rangle$ denotes the volume average of its argument. The integral in (2.15) represents the contribution of the suspended particles and is known as the particle stresslet or particle stress tensor $\boldsymbol{S}$.

3. Numerical method

Pozrikidis (1995) developed a numerical method for solving the preceding equations and implemented it in the special case where the viscosity ratio λ is equal to unity. His description of the capsule interface in global surface curvilinear coordinates has several disadvantages outlined in the introduction. In this work, we circumvent these difficulties by using an unstructured triangular grid. The present boundary-element method involves the following steps:

(1) trace the interface with a collection of marker points that define an unstructured grid of triangular elements;

(2) calculate the elastic tensions at the triangle vertices;

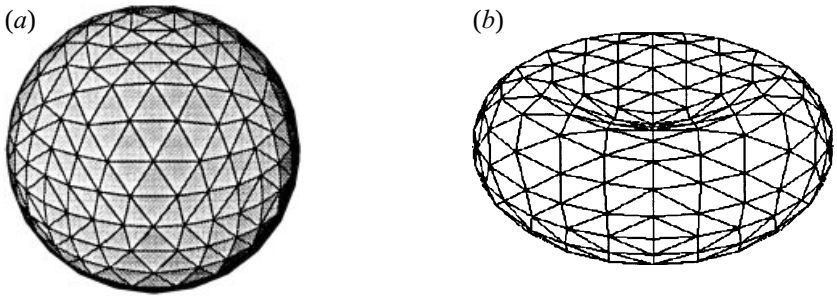

FIGURE 2. (*a*) Unstructured discretization of a sphere. (*b*) Unstructured discretization of the red blood cell's biconcave disk shape.

(3) calculate the velocity of each node by solving an integral equation using the boundary-element method;

(4) advance the position of the nodes and update their coordinates in the unstressed state for future computation of elastic tensions;

(5) return to step 2.

To discretize the unstressed interface, we subdivide each triangular face of a regular octahedron ($N_{e0} = 8$) or icosahedron ($N_{e0} = 20$) into 4^n triangular elements. The triangles are then projected radially onto a sphere to give a nearly, but not perfectly, isotropic grid of $N_e = 4^n N_{e0}$ elements, as shown in figure 2(*a*). To describe an oblate spheroid with aspect ratio b/a and yet maintain a high density of points at high-curvature areas, we use the mapping $x_{obl} = Rx$, $y_{obl} = Ry$, $z_{obl} = (b/a)Rz$ and adjust the radius R to preserve volume.

In addition to spheres and oblate spheroids, we consider the biconcave disk shape assumed by red blood cells at rest. Evans & Fung (1972) reported that the red cell shape is described in polar cylindrical coordinates by

$$z(r) = \left[1 - \left(\frac{r}{R_0}\right)\right]^{1/2} \left[C_0 + C_2\left(\frac{r}{R_0}\right)^2 + C_4\left(\frac{r}{R_0}\right)^4\right], \tag{3.1}$$

where $r \in [0, R_0]$ and $\theta \in [0, 2\pi]$. The experimentally determined coefficients R_0, C_0, C_2 and C_4 depend on the tonicity of the suspending medium. To discretize the biconcave disk, we map the grid from the surface of the sphere using the equations

$$x_{rbc} = Rx\,,\ y_{rbc} = \tfrac{1}{2}R(1-r^2)^{1/2}\left(C_0 + C_2 r^2 + C_4 r^4\right)\,,\ z_{rbc} = Rz\,, \tag{3.2}$$

where $r^2 = x^2 + z^2$ and R is adjusted to preserve the volume. Figure 2(*b*) shows the discretized shape of a healthy adult red blood cell suspended in an isotonic solution, corresponding to $C_0/R_0 = 0.207$, $C_2/R_0 = 2.003$, and $C_4/R_0 = -1.123$.

The geometry of each element is described parametrically using six nodes, three located at the vertices and three along the edges, as shown in figure 3(*a*). A grid of N_e elements requires a total of $N_p = 2N_e + 2$ nodes. A function $h(\boldsymbol{x})$ defined over the triangle, such as the position vector, is approximated by the quadratic form

$$h(\xi, \eta) = \sum_{i=1}^{6} h_i \phi_i(\xi, \eta) \tag{3.3}$$

where h_i is the value of h at node i, and the basis functions ϕ_i are given by Pozrikidis (1998). The local parametric coordinates ξ and η vary over a parametric right triangle, as shown in figure 3(*b*).

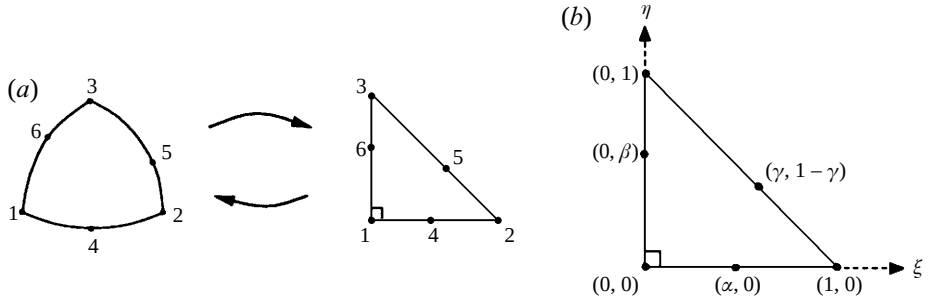

FIGURE 3. (*a*) Mapping of a curved surface triangle onto the parametric right triangle. (*b*) The six nodes of the local parametric triangle.

The elastic tension tensor for a hyperelastic membrane is computed from the Cauchy–Green strain tensor, which is determined from the surface deformation gradient, $\boldsymbol{A}$. Three vector equations are required to evaluate the three rows of $\boldsymbol{A}$. Since $\boldsymbol{A}$ acts on tangent and normal vectors according to $\mathrm{d}\boldsymbol{x} = \boldsymbol{A} \cdot \mathrm{d}\boldsymbol{X}$ and $\boldsymbol{0} = \boldsymbol{A} \cdot \boldsymbol{N}$, we require that

$$\frac{\partial \boldsymbol{x}}{\partial \xi} = \boldsymbol{A} \cdot \frac{\partial \boldsymbol{X}}{\partial \xi}, \quad \frac{\partial \boldsymbol{x}}{\partial \eta} = \boldsymbol{A} \cdot \frac{\partial \boldsymbol{X}}{\partial \eta}, \quad \boldsymbol{0} = \boldsymbol{A} \cdot \boldsymbol{N}. \tag{3.4}$$

The tangent and normal vectors are discontinuous at the element edges and nodes, causing discontinuities in $\boldsymbol{A}$. After extensive experimentation, we found that the accuracy of the simulation improves considerably if the multiple values of $\boldsymbol{A}$ are averaged at each node, weighted by the angles formed by the element edges at the point. Other averaging methods and a best-fit approach produced results of similar or inferior accuracy. Once the deformation tensor has been determined, the elastic strain and stress tensors follow from (2.5) and (2.7).

The velocity of each marker point is obtained by solving the integral equation (2.11). The surface integrals are treated as the sum of integrals over the N_e elements, yielding

$$\boldsymbol{v}(\boldsymbol{x}_0) = \frac{2}{(\lambda+1)} \boldsymbol{v}^{\infty}(\boldsymbol{x}_0) - \frac{1}{4\pi\mu(\lambda+1)} \sum_{n=1}^{N_e} \int_{E_n} \Delta \boldsymbol{f}(\boldsymbol{x}) \cdot \boldsymbol{G}(\boldsymbol{x}, \boldsymbol{x}_0)\, \mathrm{d}S(\boldsymbol{x})$$
$$+ \frac{1-\lambda}{4\pi(1+\lambda)} \sum_{n=1}^{N_e} \int_{E_n} \boldsymbol{v}(\boldsymbol{x}) \cdot \boldsymbol{\Sigma}(\boldsymbol{x}, \boldsymbol{x}_0) \cdot \boldsymbol{n}(\boldsymbol{x})\, \mathrm{d}S(\boldsymbol{x}). \tag{3.5}$$

Equation (2.2) relates the traction discontinuity multiplying the kernel of the single-layer integral to the surface divergence of the elastic stress field. Even on a structured grid where high-order differentiation is possible, numerical differentiation introduces noise and amplifies the error. On an unstructured grid, the implementation of numerical differentiation is complicated by the disordered distribution of the marker points. As an alternative to numerical differentiation, we adopt the method developed by Pozrikidis (1995) and calculate the average traction discontinuity on an element E_n with area S_n enclosed by the contour C_n from the line integral

$$\langle \Delta \boldsymbol{f} \rangle_n = -\frac{1}{S_n} \oint_{C_n} \boldsymbol{T} \cdot \boldsymbol{b}\, \mathrm{d}l. \tag{3.6}$$

The binormal vector, $\boldsymbol{b} = \boldsymbol{t} \times \boldsymbol{n}$, is the cross-product of the unit vector tangent to C and the unit normal to the surface. Equation (3.6) can be derived either by applying

the divergence theorem to (2.2) or by performing a force balance on element E_n. The stress field along the contour of an element is determined by interpolation from the nodal values, and the contour integral is computed along each edge using a Gaussian quadrature. Quadratic interpolation of the stress field causes errors in the tensions at non-vertex nodes, leading to numerical instability. With linear interpolation, only vertex-node values of the stress are required, and the stress field behaves smoothly up to significantly longer times.

Having computed the elastic tensions over all elements, the single-layer integral is expressed in terms of the average traction discontinuity by the approximation

$$\int_{E_n} \Delta \boldsymbol{f}(\boldsymbol{x}) \cdot \boldsymbol{G}(\boldsymbol{x}, \boldsymbol{x}_0)\, \mathrm{d}S(\boldsymbol{x}) \simeq \langle \Delta \boldsymbol{f} \rangle_n \cdot \int_{E_n} \boldsymbol{G}(\boldsymbol{x}, \boldsymbol{x}_0)\, \mathrm{d}S(\boldsymbol{x}), \tag{3.7}$$

which is the surface-integral equivalent of the trapezoidal rule. Since the domain of integration is closed and may thus be extended to become periodic, the Euler–McLaurin formula ensures that the integral converges with respect to the number of boundary elements at a rate that is faster than algebraic.

Using these approximations, we apply (3.5) at each node to obtain a system of N_p equations with the N_p unknown node velocities appearing on both sides of the equations. The Neumann series of the underlying integral equation converges for any finite and non-zero λ (Pozrikidis 1990), and thus the system may be solved by the method of successive substitutions. Typically, 3–50 iterations are required per velocity evaluation depending on the viscosity ratio and the size of the time-step. The rate of convergence may be accelerated by eigenvalue deflation, but this was not necessary in the present study.

Non-singular integrals are calculated using a Gaussian quadrature formula for triangular domains (Cowper 1973). The $O(1/r)$ singularity in the single-layer integral is treated by transforming the parametric triangle to polar coordinates with origin at the singular point, such that the Jacobian of the mapping exactly cancels the singularity in the integrals. To treat the singularities in the double-layer integrals, we use the desingularization method described by Pozrikidis (1992).

The nodes defining the interfacial grid can be either material points that represent infinitesimal membrane elements or simply marker points. In the first case, they move with the velocity of the fluid, whereas in the second case, they move with the component of the fluid velocity normal to the interface and with an arbitrary tangential component. A drawback of the second approach is that the unstressed positions $\boldsymbol{X}$ of the marker points must be updated according to the evolution equation

$$\frac{\mathrm{D}\boldsymbol{X}}{\mathrm{D}t} = \frac{\partial \boldsymbol{X}}{\partial t} + \boldsymbol{v} \cdot \nabla \boldsymbol{X} = \boldsymbol{0}, \tag{3.8}$$

which states that the initial position of a material point moving with the fluid velocity remains unchanged. An advantage of the second approach is that the tangential velocity field may be optimized to minimize the grid distortion (Loewenberg & Hinch 1996; Coulliette & Pozrikidis 1998). Numerical experimentation showed that the best results are obtained when the nodes are point particles; the elasticity of the interface naturally prevents large distortions, especially at low deformations.

Once the velocity of the marker points has been computed, their positions are advanced using the Runge–Kutta–Fehlberg method of orders 2 and 3 (Stoer & Bulirsch 1976; Pozrikidis 1998). This explicit integration scheme requires three velocity evaluations per time-step. The extra evaluation compared to the second-order Runge–Kutta method allows adaptive adjustment of the time-step. The additional CPU

requirement per step is outweighed by the reduction in the number of steps resulting from adaptive time-stepping.

The deformation and inclination of a deformed capsule are computed from the principal directions of the inertia tensor,

$$\boldsymbol{I} = \int_V [r^2 \boldsymbol{I} - \boldsymbol{x}\boldsymbol{x}] \mathrm{d}^3 r = \frac{1}{5} \int_{\partial V} [r^2 \boldsymbol{x}\boldsymbol{I} - \boldsymbol{x}\boldsymbol{x}\boldsymbol{x}] \cdot \boldsymbol{n} \, \mathrm{d}^2 r. \tag{3.9}$$

For numerical convenience, the divergence theorem was used to convert the volume integral to a surface integral. The deformation is then expressed in terms of the Taylor deformation parameter $D_{xy} = (L - l)/(L + l)$, where L and l are the maximum and minimum radii of the contour in the (x, y)-plane. In practice, we find it more suitable to use the deformation parameter of the triaxial ellipsoid with the same inertia tensor, which is computed using the relations

$$I_1 = (\rho V/5)(l_2^2 + l_3^2), \quad I_2 = (\rho V/5)(l_1^2 + l_3^2), \quad I_3 = (\rho V/5)(l_1^2 + l_2^2), \tag{3.10}$$

where I_i are the principal moments of inertia, and l_i are the the corresponding dimensions of the ellipsoid.

The numerical method was validated by comparing results with predictions of the small-deformation theory of Barthès-Biesel and coworkers for spherical capsules in weak flows ($G = 0.0125, 0.025$) as will be discussed in §4. Further comparison of our results with those of Pozrikidis (1995) for spherical capsules with $\lambda = 1$ and $G = 0.0125$–1.0 showed perfect agreement for the shorter times to which the latter simulations were reliable.

An octahedral discretization with 512 elements and 1026 points was used in all cases. Convergence was verified by considering several test cases under conditions of large deformations. For the octahedral discretization, symmetry about the z-coordinate plane and the z-axis was exploited to reduce the number of unknown point velocities to only one quarter of the nodes. One iteration of a full velocity evaluation requires approximately 13 s on a 266 MHz Alpha processor. A complete simulation requires anywhere from 30–1000 time-steps, each involving three velocity evaluations. Each simulation requires approximately 3–4 MB of memory.

4. Spherical capsules

Simulations were performed for capsules with spherical unstressed shapes and viscosity ratios $\lambda = 0.2$, 1.0, and 5.0. In each case, a wide range of dimensionless shear rates G was considered. For reference, the viscosity ratio of a red blood cell suspended in plasma ranges between 5 and 10, and that of a cell suspended in a standard medium used in viscometric experiments generally ranges between 0.1 and 1. In the simulations, the unstressed capsule is subjected to an impulsively started steady simple shear flow. The original intention was to compare the results from simulations performed with the zero-thickness shell formulation for the membrane with results based on the neohookean membrane. However, after completing the former simulations and embarking on the latter, it became obvious that the differences in behaviour between the two cases were negligible. Although the deformations for the neohookean membrane were slightly higher under all conditions, the maximum difference in D_{xy}, for example, was less than 3% throughout the course of the simulations, even for the most highly deformed capsules ($\lambda = 0.2$, $G = 0.45$). Therefore, we present the results obtained with the zero-thickness shell approximation, noting that these results are applicable to neohookean membranes as well.

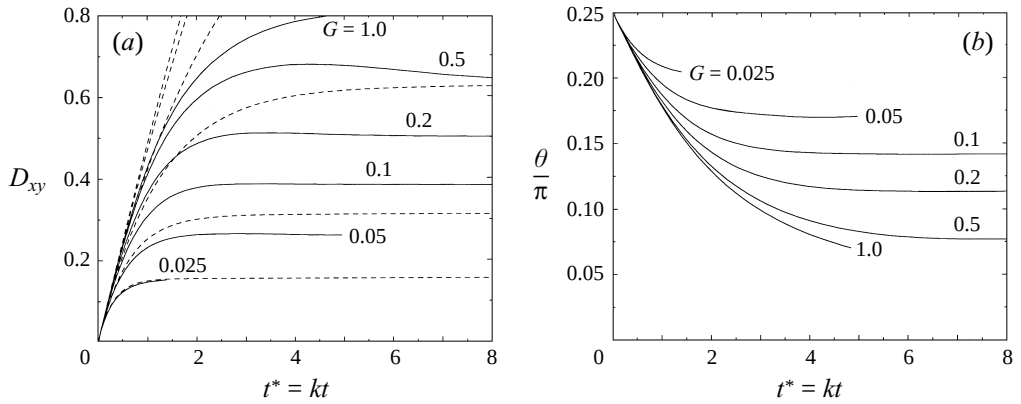

FIGURE 4. Evolution of (*a*) the deformation parameter and (*b*) inclination angle for spherical capsules with $\lambda = 1.0$. Dotted lines indicate predictions of linear perturbation theory.

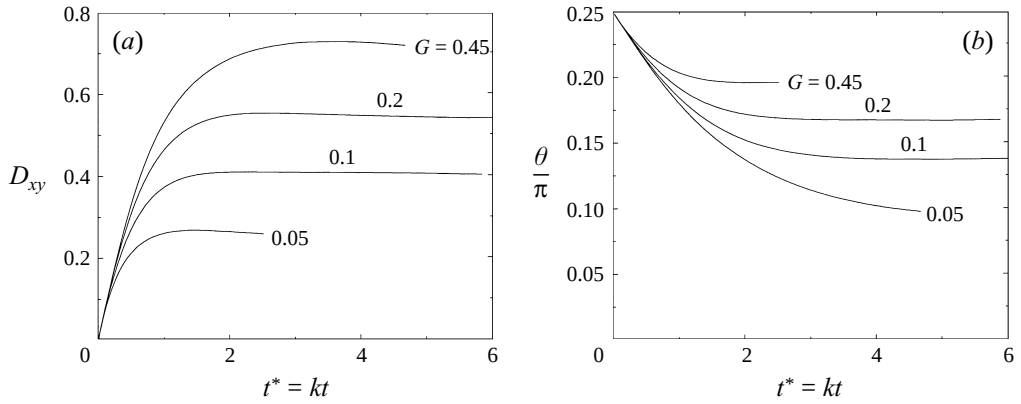

FIGURE 5. As figure 4 but with $\lambda = 0.2$.

Figures 4–6 show the evolution of the Taylor deformation parameter, D_{xy}, and inclination angle, θ, at the three values of λ. The predictions of the first-order small-deformation analysis of Barthès-Biesel & Rallison (1981) are also plotted with dashed lines for comparison. The agreement between the numerical and asymptotic results is excellent at small deformations, but worsens at moderate and large deformations. A more detailed comparison will be made later in the discussion. At low values of λ and G, the deformation and inclination curves are monotonic, but as λ or G is raised, the curves exhibit increasingly pronounced over-shoot accompanied by decaying oscillations. Corresponding analytical and numerical results for high-viscosity droplets (Cox 1969; Kennedy *et al.* 1994) also reveal decaying oscillations, in agreement with experimentally observed 'wobbling' motions.

In all cases, the capsules deform to obtain nearly ellipsoidal steady shapes that are inclined with respect to the x-axis at well-defined angles. In figure 7, we show the initial and final capsule contours in the (x, y)-plane for $\lambda = 1$ at various values of G. Figure 8 shows the profile along the capsule contour in the (x, y)-plane of the membrane tensions in the plane (T_{xy}) and normal to the plane, along the z-axis (T_z) for the relatively large deformation at $\lambda = 1$, $G = 0.5$. At high deformations, the capsules assume sigmoidal shapes familiar from experimental and numerical

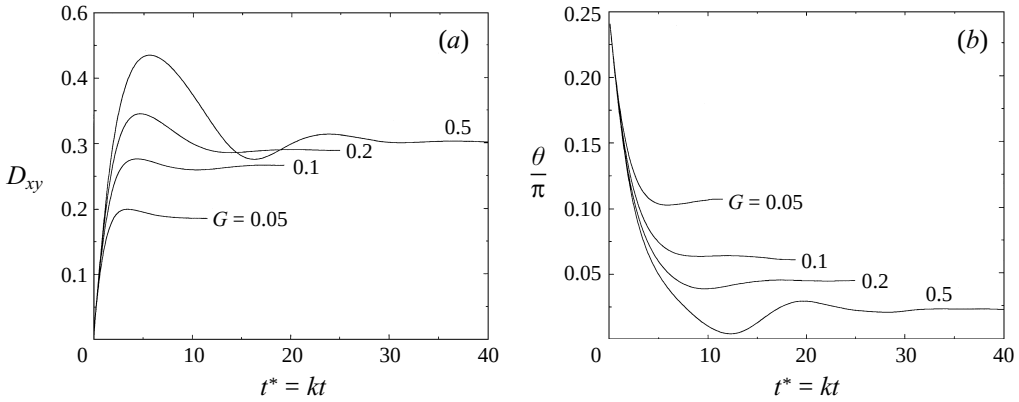

FIGURE 6. As figure 4 but with $\lambda = 5.0$.

studies of liquid drops (Taylor 1932; Kennedy *et al.* 1994). Incorporation of bending resistance would likely prevent the formation of the extreme high-curvature tips seen at $G = 1.0$; even so, the results show that the numerical method is able to handle large deformations. Figure 9 illustrates the dependence of the steady-state deformation parameter and inclination angle on G. An increase in G at constant λ or a decrease in λ at constant G raises the ratio of deforming stresses to restoring tensions and leads to greater deformations. As G is raised, the capsules elongate and tend to align with the streamlines of the unperturbed flow. Membrane rotation allows the less-viscous capsules to absorb the hydrodynamic stresses they experience while projecting across streamlines of the undisturbed flow. High internal viscosity retards the motion of the membrane, forcing the capsules to align with the flow. Thus, an increase in λ also leads to greater alignment with the flow.

For liquid drops with λ less than approximately 4, there is a critical capillary number above which the drops continue to elongate without reaching a steady state. Our results show no evidence of an analogous critical behaviour. Previously, Pozrikidis (1995) proposed the existence of a critical value of G between 0.2 and 1.0 for continued elongation of capsules with $\lambda = 1$ in simple shear flow, similar to that established by Li *et al.* (1988) for capsules in axisymmetric flow. His statement was based on small and moderate deformations of rapidly deforming capsules at high shear rates. Our results extend his findings to greater deformations and negate his proposition. The experimentally observed burst of capsules probably results instead from nonlinear membrane behaviour or material failure. Chang & Olbricht (1993*b*) noted that the site of failure of their synthetic capsules corresponded with theoretical predictions for the site of greatest membrane thinning. The numerical results of Pozrikidis (1995) later indicated that the most severe thinning coincides with the largest interfacial tensions, so burst may also have been due to material failure under high tension. In addition, we note that the synthetic capsules in Chang & Olbricht's experiments exhibited definite nonlinear behaviour including plastic deformation.

At sufficiently small deformations, our numerical results agree with the predictions of the first- and second-order small-deformation analyses of Barthès-Biesel & Rallison (1981) and Barthès-Biesel (1980), shown respectively with the solid and dashed lines in figure 9. As G is increased, the steady-state linear prediction $D_{xy} = (25/4)G$ overestimates the deformation. When $\lambda = 1$ or 0.2, the asymptotic results are accurate only for $G < 0.05$. At $\lambda = 5$, the agreement is poor even at small deformations and low

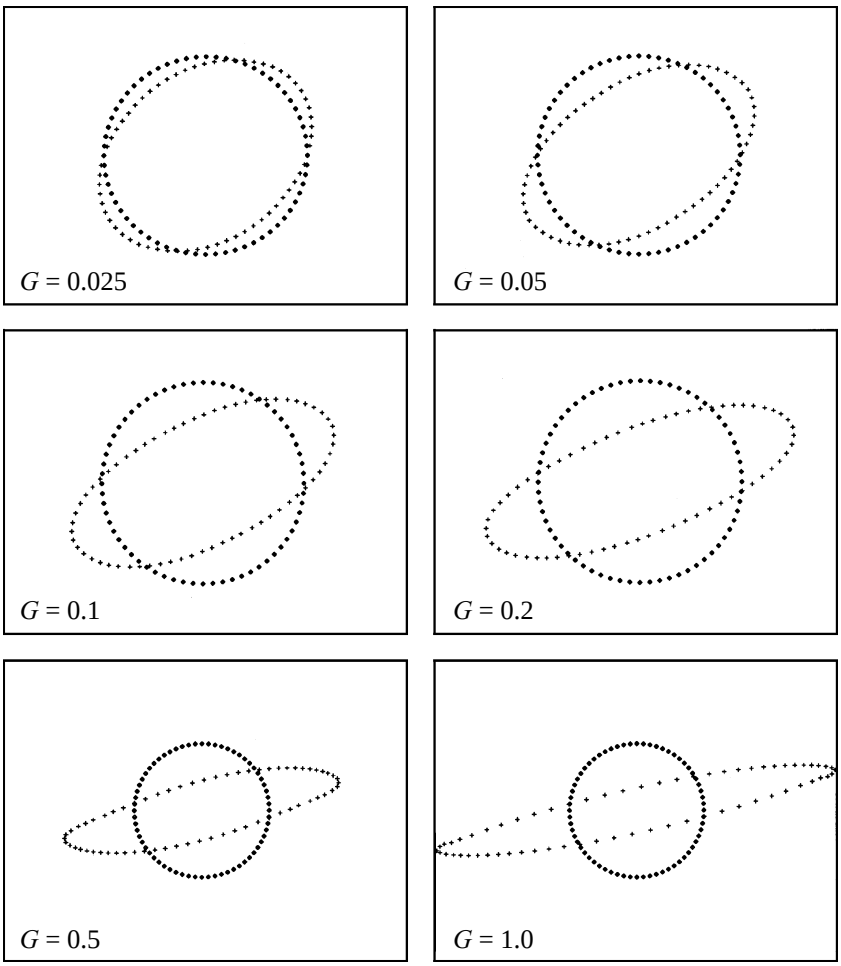

FIGURE 7. Initial and deformed contours in the (x, y)-plane of spherical capsules at various dimensionless shear rates.

shear rates. The second-order theory not only overpredicts the steady deformation, but also suggests that the deformation increases with increasing λ, which contradicts the trend seen in both experiment and simulation. The linear analysis predicts a steady inclination of $\theta = \pi/4$ in all cases. The second-order theory does indicate that the inclination decreases as λ is raised, but overpredicts the actual value for all but the smallest deformations.

Chang & Olbricht's (1993*b*) experiments with synthetic capsules also indicate that D_{xy} and θ are overestimated by the small-deformation theory. Because the experiments used capsules with appreciable membrane viscosity and $\lambda \ll 0.2$, a detailed comparison with the present numerical results is not appropriate. Despite the differences, the experimentally determined steady-state dependences of D_{xy} and θ on G are similar to those predicted by the simulations. In addition, the value of D_{xy} at which the experimental curve of D_{xy} vs. G begins to depart from the prediction of first-order theory lies between 0.2 and 0.25, which matches the value seen in figure 9 for $\lambda = 0.2$ or 1.0.

Even after a capsule has obtained a steady shape, the membrane continues to

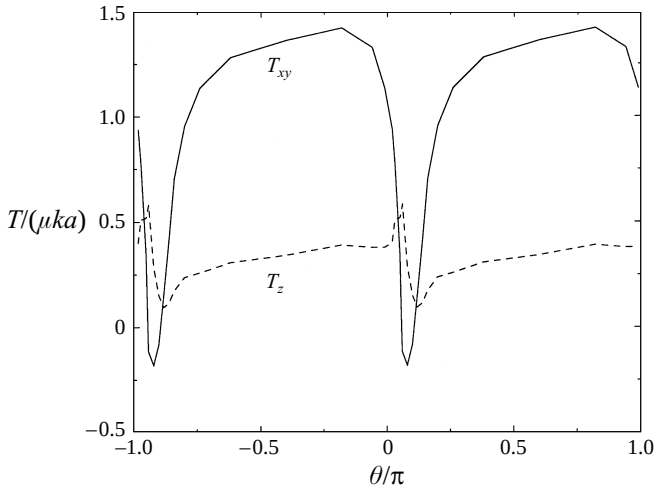

FIGURE 8. Interfacial tensions along capsule contour in the (x, y)-plane, non-dimensionalized by μka. T_{xy} represents tensions in the (x, y)-plane, and T_z represents tensions perpendicular to the plane, along the z-axis.

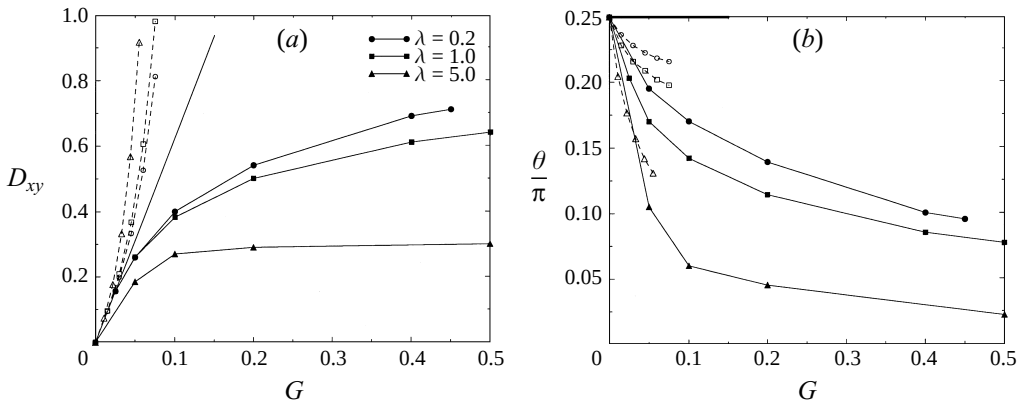

FIGURE 9. Steady-state dependence of (*a*) the deformation parameter and (*b*) inclination angle on dimensionless shear rate for initially spherical capsules with $\lambda = 0.2$, 1.0, and 5.0. Solid lines indicate predictions of first-order perturbation theory ($O(\epsilon)$). Dashed lines indicate predictions of second-order perturbation theory ($O(\epsilon^2)$).

rotate around the interior fluid in a tank-treading mode. We illustrate this behaviour in figure 10 by superimposing the trajectory of a material point on the initial and final capsule contours in the (x, y)-plane for the case $\lambda = 1$, $G = 0.2$. Eventually, the point simply travels around the steady contour in a periodic motion. In figure 11 we present the tank-treading frequencies (TTFs) at different G and λ, normalized by the corresponding frequency of rotation for a rigid sphere, $f_s = k/(4\pi)$. A linear increase of the TTF with shear rate has been seen in experimental observations of red blood cells (Fischer, Stohr-Liesen & Schmid-Schönbein 1978; Tran-Son-Tay, Sutera & Rao 1984), corresponding to a constant value of f/f_s for all G. Our simulations predict a decrease in f/f_s with G. This difference may be attributed to the area-incompressibility of the red cell membrane. In the numerical simulations, the reduction in the normalized TTF with increasing G reflects the increased contour circumference

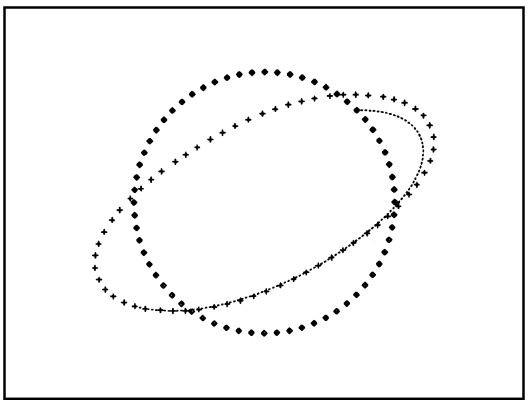

FIGURE 10. Trajectory of a single material point superimposed on initial and final contours of an initially spherical capsule with $\lambda = 1.0$ deformed at $G = 0.2$. Trajectory reflects initial deformation of capsule and subsequent tank-treading at a steady configuration.

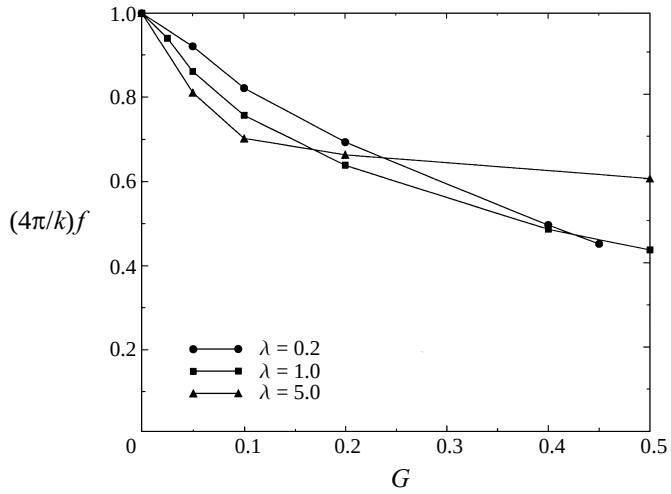

FIGURE 11. Steady-state dependence of tank-treading frequency on dimensionless shear rate for initially spherical capsules with $\lambda = 0.2$, 1.0, and 5.0.

at large deformations. At low values of G, the more-viscous internal fluid retards the motion of the membrane, and the TTF decreases with increasing λ. At high values of G, the larger deformation at lower λ reduces the TTFs, and the trend reverses.

Next, we examine the rheological properties of a dilute suspension based on the effective stresses defined in (2.15). The transient profiles of the particle shear stress and the first and second normal-stress differences for $\lambda = 1$ and $G = 0.2$ are shown in figure 12, where the stresses have been normalized by the particle shear stress for a dilute suspension of rigid spheres, $S_{xy,s} = 5k\mu/2$. The effective viscosity of the dilute suspension can be expressed in terms of the non-dimensional particle shear stress $S^*_{xy} = S_{xy}/S_{xy,s}$ as $\mu_{eff} = \mu\left(1 + \frac{5}{2}S^*_{xy}\right)$. While the linear perturbation theory predicts $S^*_{xy} = 1$ at all values of G, the numerically determined S^*_{xy} decrease with G, indicating a shear-thinning behaviour. For any given λ and G, $|\, N^*_1 \,| > |\, N^*_2 \,|$ and $N^*_2 < 0$, suggesting that the dilute suspension acts as a viscoelastic medium (Bird, Armstrong & Hassager 1977).

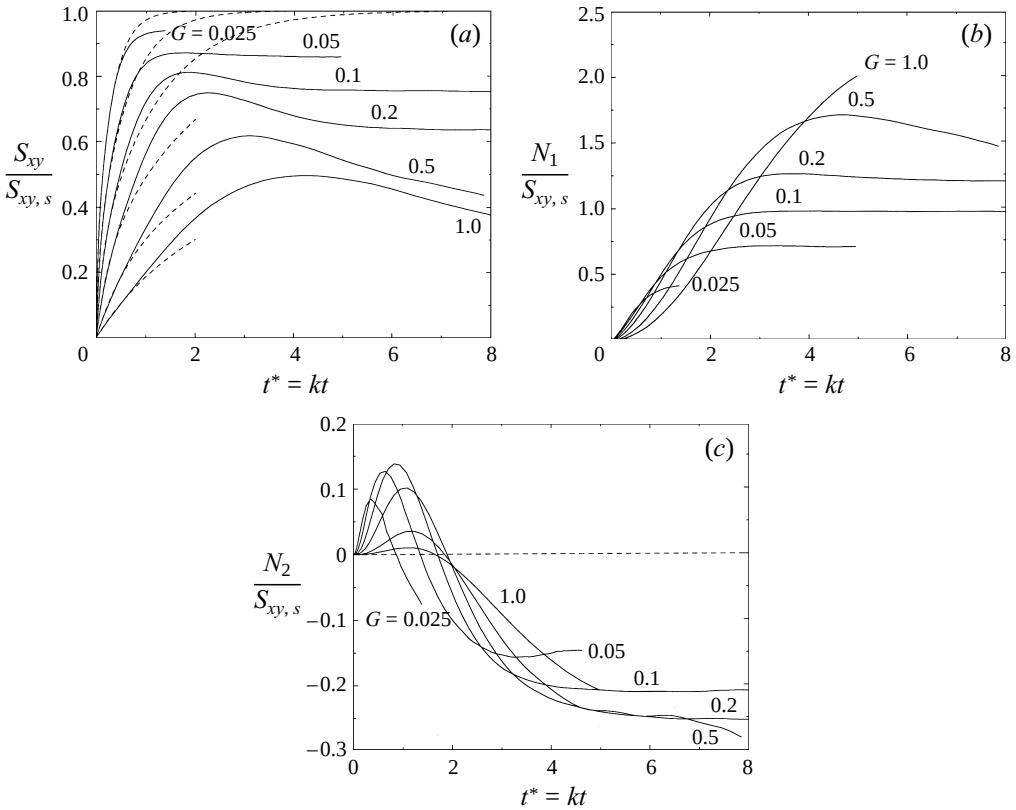

FIGURE 12. Transient profiles of normalized particle (*a*) shear stress, (*b*) first normal-stress difference, and (*c*) second normal-stress difference for initially spherical capsules with $\lambda = 1$. Dashed lines indicate predictions of linear perturbation theory.

A graph of the steady-state shear stress vs. G at the different λ, shown in figure 13, reveals shear-thinning behaviour at all values of λ. The dependence of the effective shear stress on the viscosity ratio at a fixed value of G displays a curious trend. At low shear rates, S^*_{xy} actually increases with decreasing λ, which suggests the counterintuitive result that the suspension viscosity increases as the particles become more deformable. This trend reverses at higher shear rates where the decrease in S^*_{xy} with G is steeper at lower values of λ. The unexpected trend at low G results from higher interfacial stresses and traction discontinuities across the more-deformed membranes at lower values of λ. As G is raised, the steady-state interfacial velocity increases more significantly at low λ, leading to a complete reversal of the trend by $G = 0.45$. Steady-state results for the first and second normal-stress differences are not provided here because their approach to steady values is too slow at high G to allow accurate determination.

5. Oblate spheroids and biconcave capsules

The spherical shape considered in the preceding section is an idealization of actual shapes encountered in practice. Synthetic capsules deviate from perfect spheres due to manufacturing imperfections, and resting red blood cells assume a biconcave disk configuration, resembling highly oblate spheroids with dimples on the flat sides.

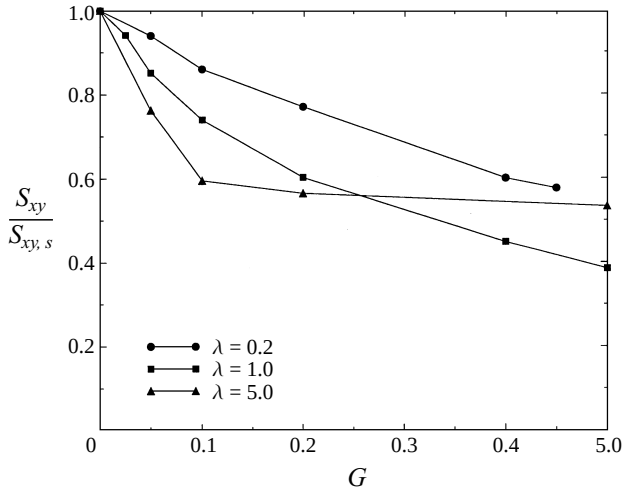

FIGURE 13. Steady-state dependence of normalized particle shear stress on dimensionless shear rate for initially spherical capsules with $\lambda = 0.2$, 1.0, and 5.0.

Because of analytical complexities, small-deformation theory has addressed only the spherical shape. Previous numerical methods (Pozrikidis 1995) proved too unstable for extended simulation of non-spherical shapes with definitive conclusions. Fortunately, the unstructured triangulation used here allows for more extensive investigations. In the series of simulations described in this section, we consider capsules with oblate shapes of various aspect ratios. For an oblate capsule of volume V, the dimensionless shear rate is defined in terms of the radius of an isovolumic sphere, $a = (3V/4\pi)^{1/3}$. Once again, we use the zero-thickness shell description of the membrane behaviour for the same reason as noted previously.

First, we consider a capsule with the nearly spherical unstressed shape of an oblate spheroid of aspect ratio $b/a = 0.9$, inclined at the angle $\theta_0 = \pi/4$ with respect to the streamlines of the unperturbed flow. Figure 14 shows the evolution of the deformation parameter and inclination angle for $\lambda = 1$ and $G = 0.05$, 0.1 and 0.2, plotted along with the corresponding evolution curves of an initially spherical capsule, indicated by dashed lines. Unlike the spherical capsule, the oblate capsule undergoes non-decaying small-amplitude oscillations in both the deformation parameter and inclination angle. The fluctuations are centred approximately at the steady-state deformation and inclination of the spherical capsule.

We investigate the origin of the fluctuations by comparing the time scale of the oscillations with the time scale of the membrane rotation. We calculate a tank-treading period, from the mean value of the TTF, and then halve it to account for the symmetry of the shape. In table 1, we compare half the membrane tank-treading period (TTP) with the period of the oscillations in the deformation parameter and inclination angle (T_{osc}) at different values of G. The agreement between the time scales supports the hypothesis that the oscillations are related to the membrane rotation. Discrepancies occur because the capsules have not established a perfectly periodic motion, especially at $G = 0.05$.

In their experimental study of synthetic capsules in shear flow, Chang & Olbricht (1993*b*) reported similar sustained small-amplitude oscillations in both D_{xy} and θ. Their capsules were nearly but not perfectly spherical; the values of D_{xy} in the unstressed state ranged between 0.02 and 0.1, encompassing the value $D_{xy} = 0.05$ for

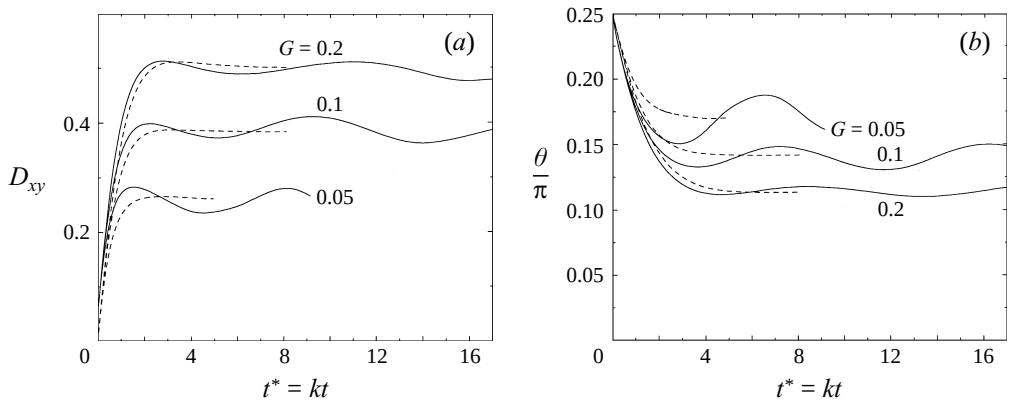

FIGURE 14. Evolution of (*a*) the deformation parameter and (*b*) inclination angle for oblate spheroidal capsules with $b/a = 0.9$ and $\lambda = 1.0$ at different dimensionless shear rates. Dashed lines indicate corresponding behaviour of initially spherical capsules.

G	$\langle \mathrm{TTF} \rangle 4\pi/k$	$k(\mathrm{TTP}/2)$	kT_{osc}
0.2	0.63	10.0	9.6
0.1	0.75	8.4	8.7
0.05	0.85	7.4	6.6

TABLE 1. Comparison of tank-treading and oscillatory time scales for initially oblate capsules with $b/a = 0.9$ and $\lambda = 1.0$.

	G	kT_{osc}	$\bar{D}_{xy}/\pi \pm \Delta$	$\bar{\theta}/\pi \pm \Delta$
Numerical	0.1	8.7	0.38±0.03	0.145±0.01
Experimental	0.1	7.4	0.38±0.04	0.17±0.04

TABLE 2. Comparison of numerically computed oscillations with those observed experimentally by Chang & Olbricht. Numerical results are for an initially oblate spheroidal capsule with $b/a = 0.9$ and $\lambda = 1.0$. Experimental results are for a nearly spherical capsule with $\lambda \ll 1.0$.

the oblate spheroid of aspect ratio 0.9. Although the viscosity ratios in the experiments were well below 1.0 and the capsules were enclosed by viscoelastic membranes, a comparison between the motions observed in the laboratory with those simulated here reveals strong similarities. Rough estimates of the periods, mean values, and magnitudes of the fluctuations observed in the experiments at a shear rate $k = 3.5\,\mathrm{s}^{-1}$ are given in table 2 alongside the results of our simulation for $G = 0.1$, $\lambda = 1$. The good agreement, despite the differences in the physical properties of the capsules, can be explained by the balancing effects of the higher surface viscosity and lower λ. The former reduces the particle deformability, while the latter increases it.

To determine the effect of the initial inclination on the subsequent deformation, we repeated the simulation for $G = 0.2$ using various initial inclinations. The results, reported by Ramanujan (1998), indicate that the initial inclination does not significantly influence the mean value, amplitude, or period of the sustained oscillations.

Chang & Olbricht (1993*b*) noted that the oscillations in the capsule motion should be distinguished from the periodic tumbling of non-spherical rigid particles undergoing Jeffery's orbits. Small-deformation analysis of capsules with viscoelastic

membranes (Barthès-Biesel & Sgaier 1985) predicts a periodic motion more akin to Jeffery's orbits as a result of reduced deformability at high surface viscosity.

Returning to figure 14, we observe that the amplitude of the oscillations decreases with increasing G; the trend is especially noticeable in the evolution of the inclination. This behaviour contrasts with the damped oscillations of spherical capsules, for which the amplitude of the oscillations becomes more pronounced as G is raised. The opposite effect of G on the oscillations of spherical and oblate capsules suggests fundamental differences in the physical origin of the oscillations. It appears that the small-scale oscillations for non-spherical unstressed shapes are different in nature from the decaying oscillations or rotational behaviours of spherical capsules, capsules with highly viscous membranes, and rigid particles. Additional simulations were performed to determine the effect of λ on the deformation and inclination. A comparison of the profiles at $\lambda = 1.0$, 5.0, and 10.0 (Ramanujan 1998) suggests that an increase in λ amplifies the oscillation, as it does for the damped oscillation of spherical capsules.

Since the values of D_{xy} and θ for a nearly spherical capsule oscillate about the corresponding values for a spherical capsule, the trends noted for spherical capsules remain applicable. An increase in G leads to greater deformation and increased alignment with the flow, whereas an increase in λ results in lower deformations but still greater alignment with the flow.

Next, we consider spheroidal capsules with more-oblate unstressed shapes of aspect ratios $b/a = 0.5$ and 0.3. In addition, we consider capsules with unstressed shapes of biconcave disks. A basis for comparing different shapes is provided by the sphericity, $s = S/(36\pi V^2)^{1/3}$, where V is the capsule volume and S is its surface area. The sphericity represents the ratio of the surface area of an isovolumic sphere to the surface area of the capsule. Since the sphere has the minimum surface area for a given volume, s is less than unity for any non-spherical shape. The sphericities of the oblate spheroids with aspect ratio 0.9 and 0.5 are respectively $s = 0.998$ and $s = 0.91$. The oblate spheroid of aspect ratio 0.3 and the biconcave disk described in §3 have comparable sphericities of 0.76 and 0.75.

Figure 15 shows the evolution of D_{xy} and θ for oblate capsules with $\lambda = 1.0$ and $G = 0.2$. Initial and deformed configurations are shown in figure 16. At long times, all capsules obtain inclined nearly ellipsoidal shapes; the dimples of the biconcave disk are smoothed out. In all cases, a material point on the membrane rotates around the capsule in an unsteady tank-treading mode. Sustained oscillations in D_{xy} and θ are seen for $b/a = 0.9$ and $b/a = 0.5$. For the spheroid with $b/a = 0.3$ and for the biconcave disk, numerical instabilities due to grid degradation limited the extent of the simulation. The results shown here reflect the reliable portion of the simulation, during which all properties including deformation, inclination, rheological properties, and interfacial tensions, vary smoothly in time/space. Despite the limited duration of the simulations, the non-monotonic inclination and deformation curves suggest that the capsules are likely to experience oscillations at later times. The amplitude and period of the oscillations appear to increase with decreasing sphericity. The behaviour of the biconcave disk is similar to that of the spheroid with $b/a = 0.3$ throughout the course of the simulation.

The simulations were repeated for $\lambda = 0.2$ and $\lambda = 5$. At $\lambda = 0.2$, the numerical method becomes unstable relatively early; however, the results are qualitatively similar to those at $\lambda = 1$ (Ramanujan 1998). The inclination and deformation profiles for $\lambda = 5$ are shown in figure 17. Although there is little change in the character of the response for the $b/a = 0.9$ spheroid, we see significant differences in the behaviour of the more-oblate capsules. For the $b/a = 0.5$ capsule, we still observe oscillations,

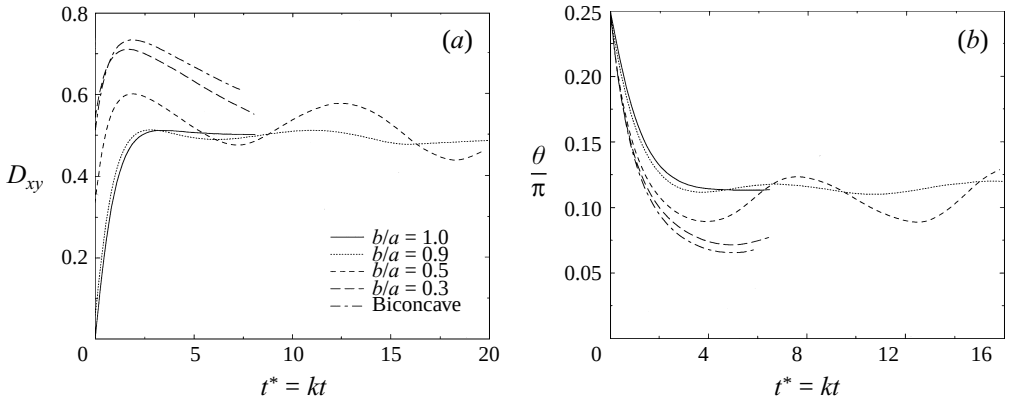

FIGURE 15. Evolution of (*a*) the deformation parameter and (*b*) inclination angle for oblate spheroidal and biconcave capsules with $\lambda = 1.0$ at $G = 0.2$.

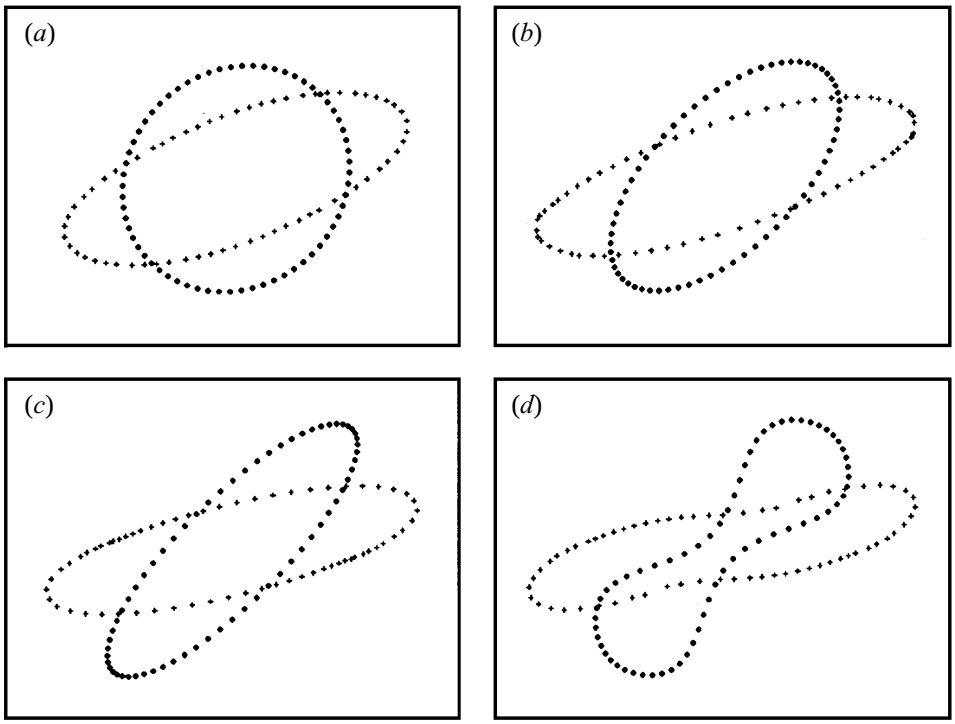

FIGURE 16. Initial and deformed contours in the (x, y)-plane of oblate spheroidal and biconcave capsules with $\lambda = 1.0$ at $G = 0.2$. Initial configurations are (*a*) $b/a = 0.9$ spheroid, (*b*) $b/a = 0.5$ spheroid, (*c*) $b/a = 0.3$ spheroid, and (*d*) biconcave disk.

but the amplitudes are larger at $\lambda = 5$ than at $\lambda = 1$, and the inclination drops below zero before increasing again. The inclination profiles for the $b/a = 0.3$ spheroid and the biconcave disk also drop below zero, but do not return to positive angles during the course of the simulations, and there is no evidence that they will do so at later times. Instead, the inclination profiles suggest continuous rotation in the clockwise direction.

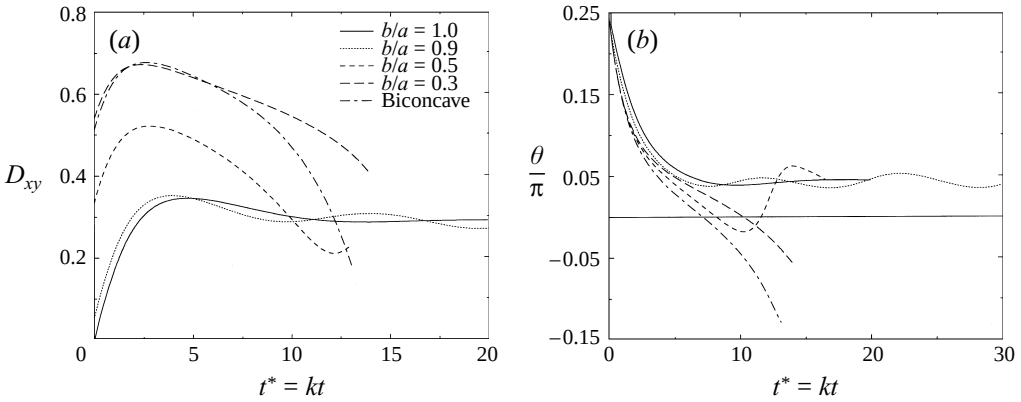

FIGURE 17. Evolution of (*a*) the deformation parameter and (*b*) inclination angle for oblate spheroidal and biconcave capsules with $\lambda = 5.0$ at $G = 0.2$.

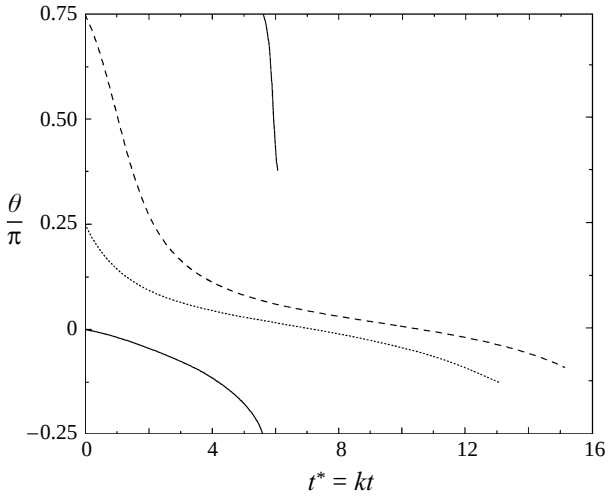

FIGURE 18. Evolution of the inclination angle for biconcave capsules with $\lambda = 5.0$ at $G = 0.2$ and various initial inclinations. Regardless of initial inclination, capsule rotates in clockwise direction only.

Additional results for the biconcave disk at various initial inclinations, shown in figure 18, also indicate clockwise rotation. Evidence of continued rotation was not seen for less-oblate and less-viscous spheroidal capsules. Plots of the capsule contours, shown in figure 19, reveal that as the capsule deforms, the dimple becomes deeper and sharper, and a cusp-like structure develops due to the absence of bending resistance. This behaviour differs from the elongation and subsequent rotation of the membrane around the interior fluid observed at lower values of λ. The monotonic inclination profiles together with the continued association of given material points with membrane features indicate that the motion is better described as simultaneous rotation and deformation rather than elongation and tank-treading. Thus, there is a transition to a rotational mode resembling the motion of rigid bodies in shear flow predicted by Jeffery (1922).

To examine this hypothesis, we consider the behaviour of the oblate capsules at $\lambda = 10$. The more oblate spheroids with $b/a = 0.5$ and $b/a = 0.3$ and the biconcave

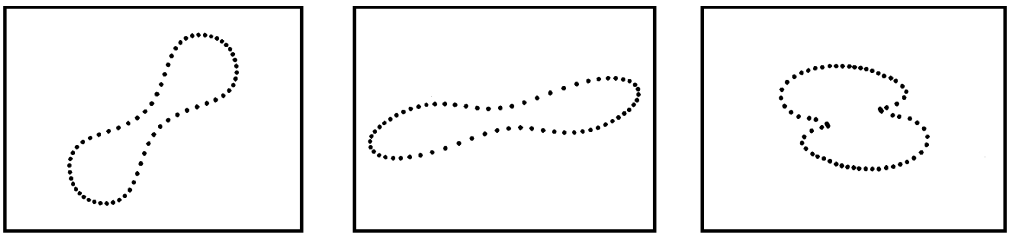

FIGURE 19. Progressive cross-sections of a biconcave discoidal capsule with $\lambda = 5.0$ deforming at $G = 0.2$. Capsule deforms and rotates continuously until the onset of instabilities.

disk undergo a well-defined continuous rotation, as illustrated in figure 20 for the biconcave disk. In figure 21 we compare the numerically determined inclination profiles for the more oblate spheroids and the biconcave disc at $\lambda = 10$ with Jeffery's predictions for the rotation of rigid oblate spheroids,

$$\tan(\theta) = \frac{-k}{r^2 + 1}(r^2 \cos^2(t) + \sin^2(t)), \tag{5.1}$$

where r is the spheroid aspect ratio. The aspect ratio of an equivalent rigid spheroid is chosen such that the theoretical orbit period,

$$T = \frac{2\pi}{k}\left(\frac{a}{b} + \frac{b}{a}\right), \tag{5.2}$$

matches the numerically obtained period of rotation. Rotation periods of $kT = 20.5$ for the biconcave disk, $kT = 30.4$ for the $b/a = 0.3$ spheroid, and $kT = 21$ for the $b/a = 0.5$ spheroid yield equivalent aspect ratios of $r_e = 0.34$, $r_e = 0.22$, and $r_e = 0.33$ respectively. The resulting inclination profiles show good agreement with the numerical results, although discrepancies exist due to capsule deformability. In experimental observations of red blood cells suspended in plasma in Poiseuille flow, Goldsmith & Marlow (1972) observed rotation of individual cells and found that Jeffery's predictions for the rotation of a rigid spheroid closely matched their data. The equivalent aspect ratio $r_e = 0.34$ determined here for the biconcave disk closely matches the value $r_e = 0.35$ determined by Goldsmith & Marlow from experimental data. The angular velocity is highest when the faces of the capsule are perpendicular to the flow direction ($\theta = \pi/2$), and lowest when they are aligned with the flow ($\theta = 0$), consistent with the 'flipping' behaviour (as opposed to steady rotation) described in experiments (Goldsmith & Marlow 1972; Schmid-Schönbein & Wells 1969). The particles are most elongated when aligned with the flow and least elongated when perpendicular to it.

The numerical simulations of non-spherical capsules showed that: (1) the nearly spherical capsule with $b/a = 0.9$ exhibits small-amplitude oscillations at all values of λ studied, (2) the $b/a = 0.5$ spheroid rotates continuously at $\lambda = 10$ but exhibits oscillations at $\lambda \leqslant 5$, and (3) the biconcave disc and the $b/a = 0.3$ spheroid undergo continuous rotation at $\lambda = 10$ and 5.0, but not at $\lambda = 1.0$ or 0.2. These results agree with previous experimental and theoretical studies which found that the viscosity ratio at which capsules switch from the rotational mode (high λ) to the elongational 'tank-treading' mode (low λ) decreases with decreasing sphericity (Bessis & Mohandas 1975; Keller & Skalak 1982; Kholeif & Weymann 1974; Morris & Williams 1978). More-oblate shapes exhibit a greater tendency to tumble. The inclination profiles of the $b/a = 0.5$ spheroid at the various λ, shown together in figure 22, illustrate how

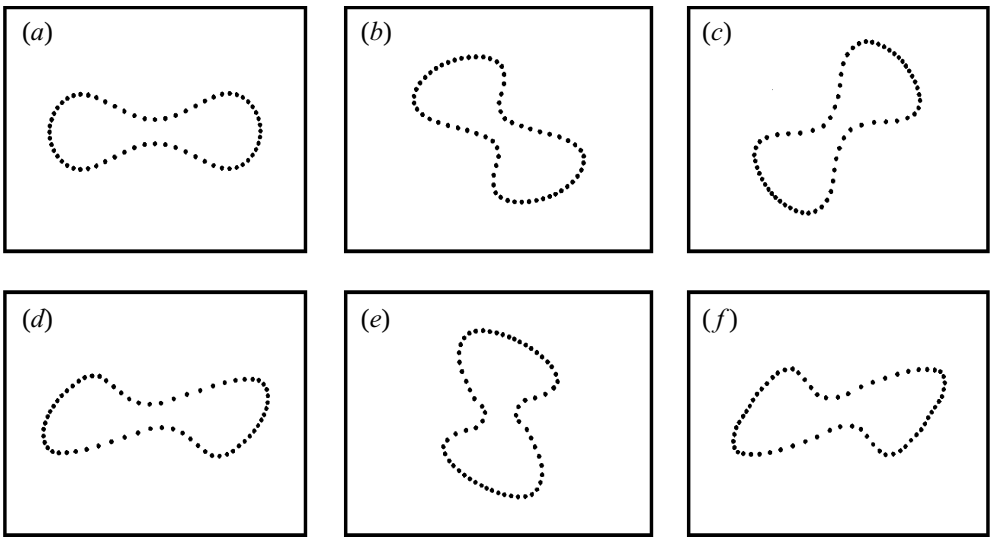

FIGURE 20. Progressive cross-sections of a biconcave disk with $\lambda = 10.0$ deforming at $G = 0.2$ Corresponding dimensionless times are $kt =$ (*a*) 0, (*b*) 3.86, (*c*) 5.64, (*d*) 10.0, (*e*) 15.86, (*f*) 19.61. Capsule rotates continuously, as would a rigid particle.

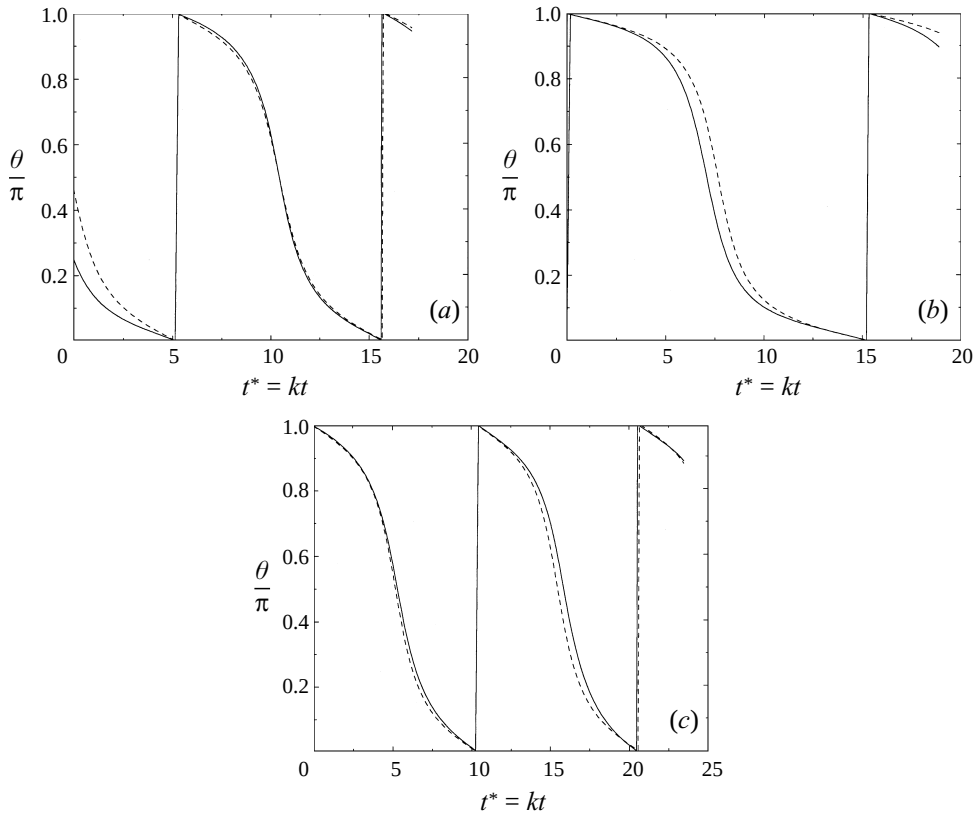

FIGURE 21. Evolution of inclination angle at $\lambda = 10.0$ and $G = 0.2$ for (*a*) $b/a = 0.5$ spheroid, (*b*) $b/a = 0.3$ spheroid, and (*c*) biconcave disk. Dashed lines indicate corresponding behaviour of rigid spheroids with $b/a = 0.33, b/a = 0.22$ and $b/a = 0.34$ respectively.

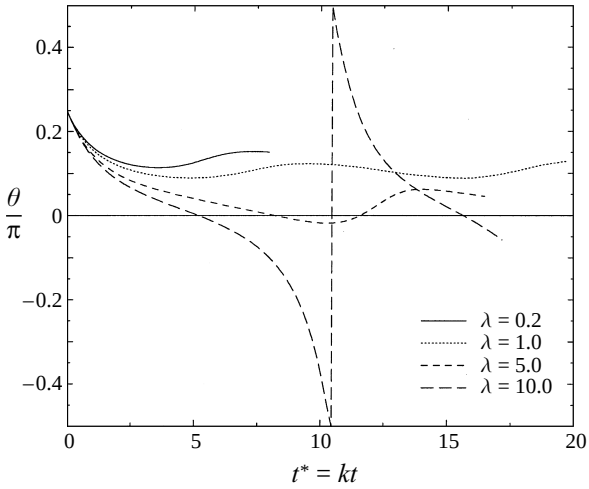

FIGURE 22. Transient profiles of inclination angle for oblate spheroidal capsules with $b/a = 0.5$ and various λ at $G = 0.2$. Capsule transitions from oscillatory to tumbling motion between $\lambda = 5.0$ and $\lambda = 10.0$.

the small-scale oscillations grow with increasing λ while their mean values decrease, leading to negative inclinations which eventually yield to continuous rotation. The smoothing of oscillations as λ is decreased and as G is increased is consistent with the observation that red cells attain apparently steady inclined configurations in viscometric flows at high shear rates in viscous suspending media (Schmid-Schönbein & Wells 1969). Although we see significant agreement between our numerical results and experimental observations of blood cells, it is important to remember that red cells deform at near constant area, with a maximum surface area expansion of 3–4% before hemolysis. In contrast, the surface area of the biconcave disks in our simulations varies by 4–25% at high-λ/low-G and low-λ/high-G respectively.

6. Discussion

Li *et al.* (1988) considered the deformation of axisymmetric capsules with $\lambda = 1$ in uniaxial stagnation-point flow. Their numerical results predicted that when the rate of elongation is increased above a critical value, the capsules continue to elongate while their cross-sections decrease, and they transform into slender threads with pointed ends. The continuous elongation despite increasing elastic tensions is possible only because the radius of the nearly cylindrical membrane diminishes in time so that the elastic force exerted on a cross-section remains finite; the elastic force is defined as the product of the axial elastic tension and the total circumferential arclength. In the case of simple shear flow, the cross-sectional area of an inclined capsule in a plane perpendicular to the major axis of deformation does not decrease rapidly enough to allow for continued elongation. This difference underlines the importance of the vorticity of the incident flow.

In the case of axisymmetric flow, when the shear rate is subcritical and a steady shape is established, the interfacial velocity vanishes, and the flow around the capsule is identical to the flow past a rigid particle with the same shape; at that point, the viscosity of the interior fluid ceases to play a role. However, the interior viscosity can still affect the approach to steady state and the stability of the steady shape.

To investigate the issue of stability, we implemented a boundary-integral method for axisymmetric flow and extended the results of Li *et al.* (1988) to viscosity ratios other than unity. The results showed that the critical shear rate for $\lambda = 10$ is only slightly higher than that for $\lambda = 1$, and that for $\lambda = 1$ is somewhat lower than that for $\lambda = 0.1$. Thus the viscosity ratio has a measurable but not a profound effect on the ability of a capsule to establish a steady shape in axisymmetric flow.

Returning to simple shear flow, we note that nearly spherical capsules with low to moderate internal-to-external viscosity ratios exhibit small-scale oscillations in the deformation and inclination. These results agree qualitatively and quantitatively with the experimental observations of synthetic capsules by Chang & Olbricht (1993*b*). The oscillatory behaviour is a feature unique to non-spherical unstressed shapes. The spherical capsule represents a special case where the surface points are completely indistinguishable, allowing the capsule to maintain a steady configuration even as the membrane tank-treads. In contrast, the material points on the membrane of the non-spherical capsule are distinguished by their location on the unstressed shape. Thus, rotation of the membrane affects the interfacial velocity field, and a steady tank-treading behaviour cannot be established. Instead, we observe small-scale oscillations related to the membrane rotation.

As the sphericity of the unstressed shape decreases or its internal viscosity increases, the small-scale oscillations grow and give way to continuous rotation, accurately described by Jeffery's results for rigid bodies in shear flow. The tendency of more-oblate particles to rotate, the value of the viscosity ratio at which the more-oblate capsules are predicted to undergo rotation, and the predicted periods of rotation all match experimental observations of red blood cells. Finally, the smoothing of the oscillations as the viscosity ratio is decreased or as the shear rate is increased agrees with observations that red cells obtain apparently steady configurations in viscometric shear flow.

The boundary-element method developed in this work significantly improves our ability to simulate capsules with hyperelastic membranes, enabling us to study moderate to large deformations of spherical and oblate shapes. Even with the improvements in the numerical method, numerical instability resulting from degradation of the grid and the neglect of bending resistance are problematic under conditions of high and low deformations, respectively. The development of adaptive grid regeneration using the advancing-front method is the topic of a current investigation.

This research is supported by the National Science Foundation, the SUN Microsystems Corporation, and the Wisconsin Alumni Research Foundation. Partial support is provided by the donors of the Petroleum Research Fund, administered by the Americal Chemical Society. The authors express their appreciation to Sangtae Kim and Chad Coulliette for many helpful discussions.

REFERENCES

Barthès-Beisel, D. 1980 Motion of spherical microcapsule freely suspended in a linear shear flow. *J. Fluid Mech.* **100**, 831–853.

Barthès-Biesel, D. & Rallison, J. M. 1981 The time-dependent deformation of a capsule freely suspended in a linear shear flow. *J. Fluid Mech.* **113**, 251–256.

Barthès-Biesel, D. & Sgaier, H. 1985 Role of membrane viscosity in the orientation and deformation of a spherical capsule suspended in shear flow. *J. Fluid Mech.* **160**, 119–135.

Beatty, M. F. 1987 Topics in finite elasticity: hyperelasticity of rubber, elastomers, and biological tissues–with examples. *Appl. Mech. Rev.* **40**, 1699–1734.

Bessis, M. & Mohandas, N. 1975 Deformability of normal, shape-altered and pathological red cells. *Blood Cells* **1**, 315–321.

Bird, R. B., Armstrong, R. C. & Hassager, O. 1977 *Dynamics of Polymeric Liquids I. Fluid Dynamics.* John Wiley and Sons.

Boussinésq, X. 1913 Sur l'existence d'une viscosité superficielle, dans la mince couche de transition séparant un liquide d'un autre fluide contigu. *Ann. Chim. (Phys.)* **29**, 349–357.

Chang, K. S. & Olbricht, W. L. 1993*a* Experimental studies of the deformation of a synthetic capsule in extensional flow. *J. Fluid Mech.* **250**, 587–608.

Chang, K. S. & Olbricht, W. L. 1993*b* Experimental studies of the deformation and breakup of a synthetic capsule in steady and unsteady simple shear flow. *J. Fluid Mech.* **250**, 609–633.

Charles, R. & Pozrikidis, C. 1998 Significance of the dispersed phase viscosity on the simple shear flow of suspensions of two-dimensional liquid drops. *J. Fluid Mech.* (In Press).

Coulliette, C. & Pozrikidis, C. 1998 Motion of an array of drops through a cylindrical tube. *J. Fluid Mech.* **358**, 1–28.

Cowper, G. R. 1973 Gaussian quadrature formulas for triangles. *Intl J. Numer. Meth. Engng* **7**, 405–408.

Cox, R. G. 1969 The deformation of a drop in general time-dependent fluid flow. *J. Fluid Mech.* **37**, 601–623.

Evans, E. & Fung, Y. C. 1972 Improved measurements of the erythrocyte geometry. *Microvasc. Res.* **4**, 335–347.

Evans, E. & Skalak, R. 1980 *Mechanics and Thermodynamics of Biomembranes.* CRC Press.

Fischer, T. M., Stohr-Liesen, M. & Schmid-Schönbein, H. 1978 The red cell as a fluid droplet: tank tread-like motion of the human erythrocyte membrane in shear flow. *Science* **202**, 894–896.

Goldsmith, H. L. & Marlow, J. 1972 Flow behaviour of erythrocytes: 1. rotation and deformation in dilute suspensions. *Proc. R. Soc. Lond.* B **182**, 351–384.

Jeffery, G. B. 1922 The motion of ellipsoidal particles immersed in a viscous fluid. *Proc. R. Soc. Lond.* A **102**, 161–179.

Keller, S. R. & Skalak, R. 1982 Motion of a tank-treading ellipsoidal particle in a shear flow. *J. Fluid Mech.* **120**, 27–47.

Kennedy, M. R., Pozrikidis, C. & Skalak, R. 1994 Motion and deformation of liquid drops, and the rheology of dilute emulsions in simple shear flow. *Computers & Fluids* **23**(2), 251–278.

Kholeif, I. A. & Weymann, H. D. 1974 Motion of a single red blood cell in plane shear flow. *Biorheology* **11**, 337–348.

Leyrat-Maurin, A. & Barthès-Biesel, D. 1994 Motion of a deformable capsule through a hyperbolic constriction. *J. Fluid Mech.* **279**, 135–163.

Leyrat-Maurin, A., Drochon, A. & Barthès-Biesel, D. 1993 Flow of a capsule through a constriction: application to cell filtration. *J. Phys. III France* **3**, 1051–1056.

Li, X., Charles, R. & Pozrikidis, C. 1996 Simple shear flow of suspensions of liquid drops. *J. Fluid Mech.* **320**, 1–18.

Li, X. Z., Barthès-Biesel, D. & Helmy, A. 1988 Large deformations and burst of a capsule freely suspended in an elongational flow. *J. Fluid Mech.* **187**, 179–196.

Loewenberg, M. & Hinch, E. J. 1996 Numerical simulation of a concentrated suspension in shear flow. *J. Fluid Mech.* **321**, 395–419.

Morris, D. R. & Williams, A. R. 1978 The effects of suspending medium viscosity on erythrocyte deformation and haemolysis in vitro. *Biochimica Biophysica Acta* **550**, 288–296.

Pozrikidis, C. 1990 The instability of a moving viscous drop. *J. Fluid Mech.* **210**, 1–21.

Pozrikidis, C. 1992 *Boundary Integral and Singularity Methods for Linearized Viscous Flow.* Cambridge University Press.

Pozrikidis, C. 1994 Effects of surface viscosity on the finite deformation of a liquid drop and the rheology of dilute emulsions in simple shearing flow. *J. Non-Newtonian Fluid Mech.* **51**, 161–178.

Pozrikidis, C. 1995 Finite deformation of liquid capsules enclosed by elastic membranes in simple shear flow. *J. Fluid Mech.* **297**, 123–152.

Pozrikidis, C. 1998 *Numerical Computation in Science and Engineering.* Oxford University Press.

Ramanujan, S. 1998 Numerical simulations of capsule deformation in shear flows. PhD thesis, University of Wisconsin – Madison.

Schmid-Schönbein, H. & Wells, R. 1969 Fluid drop-like transition of erythrocytes under shear. *Science* **165**, 288–291.

Scriven, L. E. 1960 Dynamics of a fluid interface. *Chem. Engng Sci.* **12**, 98–108.

Shrivatsava, S. & Tang, J. 1993 Large deformation finite element analysis of non-linear viscoelastic membranes with reference to thermoforming. *J. Strain Anal.* **28**, 31–51.

Skalak, R., Dong, C. & Zhu, C. 1990 Passive deformations and active motions of leukocytes. *J. Biomech. Engng* **112**, 295–302.

Skalak, R.,Tozeren, A., Zarda, R. P. & Chien, S. 1973 Strain energy function of red blood cell membranes. *Biophys. J.* **245**, 245–264.

Stoer, J. & Bulirsch, R. 1976 *Introduction to Numerical Analysis.* Springer.

Taylor, G. I. 1932 The viscosity of a fluid containing small drops of another fluid. *Proc. R. Soc. Lond.* A **138**, 41–48.

Tran-Son-Tay, R., Sutera, S. P. & Rao, P. R. 1984 Determination of red blood cell membrane viscosity from rheoscope observations of tank-treading motion. *Biophys. J.* **46**, 65–72.